



# Sodium dodecyl sulfate-assisted hydrothermal synthesis of mesoporous nickel cobaltite nanoparticles with enhanced catalytic activity for methanol electrooxidation

Rui Ding<sup>a,b,c,\*</sup>, Li Qi<sup>a</sup>, Mingjun Jia<sup>c</sup>, Hongyu Wang<sup>a,\*</sup>

<sup>a</sup>State Key Laboratory of Electroanalytical Chemistry, Changchun Institute of Applied Chemistry, Chinese Academy of Sciences, 5625 Renmin Street, Changchun 130022, China

<sup>b</sup>Graduate University of Chinese Academy of Sciences, Beijing 100039, China

<sup>c</sup>State Key Laboratory of Theoretical and Computational Chemistry, College of Chemistry, Jilin University, Changchun 130023, China

## H I G H L I G H T S

- SDS enhances mesoporous structures and surface electroactive sites.
- SDS-assisted NiCo<sub>2</sub>O<sub>4</sub> electrode shows faster electrochemical kinetics.
- SDS-assisted NiCo<sub>2</sub>O<sub>4</sub> electrode exhibits enhanced electrocatalytic activity.
- Surface physicochemical properties strongly affect electrocatalytic behavior.

## A R T I C L E I N F O

### Article history:

Received 6 September 2013

Received in revised form

1 November 2013

Accepted 21 November 2013

Available online 1 December 2013

### Keywords:

Nickel cobaltite

Methanol oxidation reaction

Electrocatalysts

Fuel cells

Mesoporous

Soft-template

## A B S T R A C T

Mesoporous nickel cobaltite (NiCo<sub>2</sub>O<sub>4</sub>) nanoparticles have been synthesized via a facile hydrothermal strategy with the assistance of sodium dodecyl sulfate (SDS) soft template (ST). Their physicochemical properties have been characterized via X-ray diffraction (XRD), scanning electron microscopy (SEM) and energy-dispersive X-ray spectra (EDS), transmission electron microscopy (TEM), X-ray photoelectron spectra (XPS) and nitrogen sorption measurements. Their electrocatalytic performances have been examined by cyclic voltammetry (CV), linear sweep voltammetry (LSV), chronoamperometry (CA) and electrochemical impedance spectroscopy (EIS) tests. The obtained NiCo<sub>2</sub>O<sub>4</sub> materials exhibit a typical nanoscale crystalline hexagonal morphology with specific surface area (SSA) and mesopore volume of 88.63 m<sup>2</sup> g<sup>−1</sup> and 0.298 cm<sup>3</sup> g<sup>−1</sup>. Impressively, the SDS-assisted NiCo<sub>2</sub>O<sub>4</sub> electrode shows a catalytic current density of 125 mA cm<sup>−2</sup> and 72% retention for consecutive 1000 s at 0.6 V in 1 M KOH and 0.5 M CH<sub>3</sub>OH electrolytes towards methanol (CH<sub>3</sub>OH) electrooxidation, which is better than the one without SDS assistance. The pronounced electrocatalytic activity is largely ascribed to their higher surface intensities of Co and Ni species and superior mesoporous nanostructures, which provide the richer electroactive sites and faster electrochemical kinetics, leading to the enhanced electrocatalytic activity.

© 2013 Elsevier B.V. All rights reserved.

## 1. Introduction

Environmental pollution, climate change, and exhaust of fossil fuels have triggered the ever-growing worldwide interest in developing sustainable and clean energy devices [1,2]. Direct methanol fuel cells (DMFCs) have been regarded as a promising candidate for future energy demand, largely owing to their high

energy conversion efficiency, low operating temperature and light pollutant emission [3]. DMFCs are generally divided into two categories according to whether the electrolyte is acidic or alkaline. Alkaline DMFCs have usually aroused more interest than the acid one due to the potential use of lower-cost non-Pt catalysts to achieve faster kinetics of both oxygen reduction reaction (ORR) and methanol oxidation reaction (MOR) in alkaline medium [4]. The use of non-Pt catalysts can substantially reduce the cost of the fuel cell system. Moreover, the less-corrosive nature of an alkaline environment ensures a potential greater longevity.

One of the key requirements for alkaline DMFCs is to explore highly efficient and much cheaper anode catalysts for MOR to

\* Corresponding authors. State Key Laboratory of Electroanalytical Chemistry, Changchun Institute of Applied Chemistry, Chinese Academy of Sciences, 5625 Renmin Street, Changchun 130022, China. Tel./fax: +86 431 85262287.

E-mail addresses: [drm8122@163.com](mailto:drm8122@163.com), [dingrui@ciac.ac.cn](mailto:dingrui@ciac.ac.cn) (R. Ding), [hongyuwang@ciac.ac.cn](mailto:hongyuwang@ciac.ac.cn) (H. Wang).

replace the traditional noble metal catalysts including platinum (Pt) [5–9], palladium (Pd) [10–13], ruthenium (Ru) [14] and their alloys [9,15–17]. Thus, much efforts in the search for alternative low-cost transition metal oxides catalysts, such as NiO [18–20],  $\text{Co}_3\text{O}_4$  [21],  $\text{MnO}_x$  [22], etc. have been devoted in recent years in the fuel cell community. Unfortunately, the comparatively low electronic conductivity and poor catalytic activity of these metal oxides hinder their further applications. As a result, it is still a key challenge to explore novel metal oxides catalysts with high conductivity and catalytic activity for MOR.

It is reported that transition metal based composite materials, such as dioxides, perovskites, pyrochlores, and spinel-type oxides, usually exhibit synergistic enhancement in catalytic activities that are much better than a simple combination of individual components, exhibiting promising properties with respect to chemical activity, stability, or resistance to poisoning [23]. Of which, cobalt-containing spinel-type oxides ( $\text{MCo}_2\text{O}_4$ , where M = Ni, Mn, Zn, Cu, Mg, etc.) have attracted considerable attention due to their superior activity, easy availability, high thermodynamic stability, and low electrical resistance [24,25]. It is well-known that spinel bimetallic oxide nickel cobaltite ( $\text{NiCo}_2\text{O}_4$ ) possesses richer redox chemistry (both Ni and Co active species), much better electronic conductivity (at least two orders of magnitude higher) than nickel oxide and cobalt oxide [26,27], and the  $\text{NiCo}_2\text{O}_4$  materials have already shown excellent electrocatalytic activities in many electrode reactions, for example:  $\text{Cl}_2$  evolution reaction (CER) [28],  $\text{O}_2$  evolution reaction (OER) [27,29],  $\text{O}_2$  reduction reaction (ORR) [30,31],  $\text{H}_2\text{O}_2$  reduction reaction (HRR) [32–34], etc. The recent researches have shown that the spinel  $\text{NiCo}_2\text{O}_4$  materials exhibit also a high catalytic activity towards MOR [33–36]. However, to further enhance their activity remains very meaningful for the promotion of high-performance non-Pt catalysts based alkaline DMFCs.

Sodium dodecyl sulfate (SDS)-assistant soft-template (ST) method is regarded as an effective technique to fabricate functional mesoporous nanomaterials via the oil-water interface self-assembly process between organic phase and inorganic precursors [37]. Moreover, hydrothermal technique is a desirable method to synthesize superior crystalline nanoparticles due to its unique temperature and pressure environments. Therefore, a combination of these two techniques can be expectable to obtain advanced electrocatalysts for MOR.

In this work, mesoporous  $\text{NiCo}_2\text{O}_4$  nanoparticles were synthesized via a facile hydrothermal method with the assistance of SDS template. Their physicochemical properties were characterized, and further their electrocatalytic behavior towards MOR was investigated, which shows a high catalytic activity and stability, and thus a promising application.

## 2. Experimental

### 2.1. Synthesis of materials

All the reagents in the experiment are of analytical grade and were used without further purification. Firstly,  $\text{Co}(\text{NO}_3)_2 \cdot 6\text{H}_2\text{O}$  (0.67 g),  $\text{Ni}(\text{NO}_3)_2 \cdot 6\text{H}_2\text{O}$  (0.33 g) and SDS (1.0 g) were dissolved in distilled water (20 mL) under continuous magnetic stirring for 30 min to form a homogenous solution. Next, NaOH (0.3 M, 22 mL) aqueous solution was poured into the above generated solution under continuous stirring for another 30 min to form a well-mixed solution. Then, the resulting solution was transferred into a teflon-lined stainless-steel autoclave (50 mL in volume) and heated at  $140^\circ\text{C}$  for 12 h in a box oven, and then cooled naturally to the room temperature. The product was collected by centrifugal filtration, washed with distilled water and absolute ethanol several times, and next dried at  $60^\circ\text{C}$  for 12 h in a

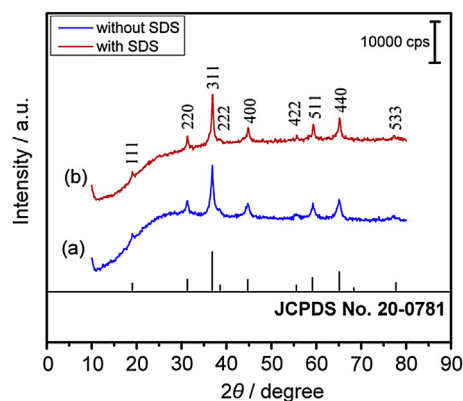


Fig. 1. XRD patterns of  $\text{NiCo}_2\text{O}_4$  materials without (a) and with (b) SDS.

vacuum oven, afterward ground finely using a mechanical grinder, and finally calcined at  $300^\circ\text{C}$  for 3 h in air atmosphere at a heating rate of  $1^\circ\text{C min}^{-1}$  in a muffle stove to obtain the ultimate  $\text{NiCo}_2\text{O}_4$  materials. For comparison, the  $\text{NiCo}_2\text{O}_4$  materials without SDS addition were also prepared through the same procedure.

### 2.2. Materials characterizations

X-ray diffraction (XRD) patterns were recorded on a Rigaku-Dmax 2500 diffractometer equipped with graphite monochromatized Cu  $K\alpha$  radiation source ( $\lambda = 1.5406 \text{ \AA}$ ) at a scanning speed of  $4^\circ \text{ min}^{-1}$  in the  $2\theta$  range of  $10^\circ$ – $80^\circ$ . Scanning electron microscopy (SEM) images and energy-dispersive X-ray spectra (EDS) were observed using a Philips XL 30 and JEOL JSM-6700F microscope. Transmission electron microscopy (TEM) images were carried out with Hitachi model H-8100 operating at 200 kV accelerating voltage. X-ray photoelectron spectra (XPS) were measured by using an ESCALAB-MKII spectrometer (UK) with Al  $K\alpha$  radiation (1486.6 eV), and the raw spectra were curve-fitted by non-linear least squares fittings with a Gauss–Lorentz ratio (80:20) through the XPSPEAK41 software. Nitrogen sorption measurements were determined at 77 K using a Micromeritics ASAP 2020 Analyzer, prior to analysis, the samples were degassed under vacuum at  $120^\circ\text{C}$  for 24 h, the specific surface area (SSA) was calculated using the multipoint Brunauer–Emmett–Teller (BET) method, the pore size distribution (PSD) and pore volume data were calculated from the desorption branches based on the Barrett–Joyner–Halenda (BJH) equation.

### 2.3. Electrode fabrication and electrochemical measurements

The  $\text{NiCo}_2\text{O}_4$  electrodes were fabricated by pressing the mixture of 66.7 wt% active materials (as-synthesized  $\text{NiCo}_2\text{O}_4$ ) and 33.3 wt% conductive binder (teflonized acetylene black, TAB, the mass ratio of AB and PTFE is 2:1) onto the stainless steel mesh current collector. The mass loading of active materials was about  $6 \text{ mg cm}^{-2}$ .

The electrocatalytic performances of  $\text{NiCo}_2\text{O}_4$  electrodes were examined by cyclic voltammetry (CV), linear sweep voltammetry (LSV), chronoamperometry (CA) and electrochemical impedance spectroscopy (EIS) tests in a conventional three-electrode cell containing a  $\text{NiCo}_2\text{O}_4$  working electrode (WE), a platinum plate ( $3 \text{ cm} \times 4 \text{ cm}$ ) counter electrode (CE), and a Hg/HgO (1 M KOH, aqueous) reference electrode (RE). EIS experiments were taken under open circuit voltage (OCV) with the alternating current (ac) amplitude of 5 mV over frequency range of 100 KHz–10 mHz. The electrolytes for MOR tests were 1 M KOH with different

concentrations of CH<sub>3</sub>OH (0.3–0.9 M). All the tests were carried out at room temperature (about 25 °C).

### 3. Results and discussion

#### 3.1. Physicochemical properties of the NiCo<sub>2</sub>O<sub>4</sub> materials

Fig. 1 shows the XRD patterns of as-synthesized NiCo<sub>2</sub>O<sub>4</sub> materials. Their resultant diffraction peaks corroborate with the standard patterns for cubic spinel NiCo<sub>2</sub>O<sub>4</sub> crystalline phase (JCPDS No. 20-0781). The largely sharp and narrow diffraction lines of both samples illustrate their good crystallinity, which can be attributable to the unique hydrothermal environments for crystal growth. Note that the particles with SDS possess a lightly higher crystallinity due to their better defined peaks and this can be easily judged from (220) and (440) crystal planes, which can be also verified by their TEM observations discussed later. The lattice parameter ( $a_0$ ) values for the cubic lattice NiCo<sub>2</sub>O<sub>4</sub> unit cell of both samples, determined from the observed  $d$ -spacing for crystal plane (311) at  $2\theta$  value of  $36.8^\circ$  by using Eqs. (1) and (2), are calculated to be 0.8104 nm, which is close to the standard value of 0.8110 nm for NiCo<sub>2</sub>O<sub>4</sub> (JCPDS No. 20-0781), indicating the successful incorporation of Ni into the lattice of Co<sub>3</sub>O<sub>4</sub>.

$$a_0 = d(h^2 + k^2 + l^2)^{\frac{1}{2}} \quad (1)$$

$$2d \sin \theta = \lambda \quad (2)$$

where  $\lambda$  is the wavelength of X-ray radiation (1.5406 Å),  $\theta$  is the Bragg angle of diffraction,  $d$  is observed space for crystal plane (311),  $h$ ,  $k$ ,  $l$  are the Miller indices.

The SEM images and EDS patterns of as-synthesized NiCo<sub>2</sub>O<sub>4</sub> materials are depicted in Fig. 2. The observed NiCo<sub>2</sub>O<sub>4</sub> particles exhibit a typical hexagonal morphology with most of particle size locating in the range of 100–200 nm for the one without SDS and 50–150 nm for the one with SDS, showing a good nanoscale crystalline morphology, which corresponds well with their XRD results. In addition, both materials display a loosely stacked porous structure, and this can facilitate the ion/electron transportation process at and within the electrode/electrolyte interface, which is a very important factor for boost of electrochemical kinetics and catalytic activity of the catalysts. The EDS tests were also conducted accompanying with the SEM observations to monitor their

chemical compositions and the results are listed in Fig. 2c and f. It demonstrates that both NiCo<sub>2</sub>O<sub>4</sub> materials exhibit the intrinsic O, Co and Ni elements. Herein, the signals of Si element originated from the silicon plate as support during the measurement, and Au was used in order to enhance the surface conductivity of the materials for the analysis and is also visible in the EDS patterns.

The surface morphology and crystalline structure of as-synthesized NiCo<sub>2</sub>O<sub>4</sub> materials were also investigated by TEM measurements which are shown in Fig. 3. The particles without SDS (Fig. 3a and b) present a typical hexagonal image with a stacked structure. Moreover, the particles in size ranges of 100–150 nm were easily observed and the edge thickness of the particles is estimated to be 20 nm. The particles with SDS (Fig. 3d and e) exhibit a similar image to the one without SDS, but the size is much smaller and only the ones in size of less than 100 nm are observed in the scope of detecting region, furthermore, it is difficult to discern their exact edge size, indicating the particles with SDS tend to be a thinner image, which may be due to the enclosure function of micelles formed by SDS template in the synthesis that can prohibit the growth of the ultimate NiCo<sub>2</sub>O<sub>4</sub> particles. The selected area electron diffraction (SAED) patterns (Fig. 3c and f) display the typical diffraction rings for crystal planes of spinel NiCo<sub>2</sub>O<sub>4</sub> (JCPDS 20-0781), indicating the polycrystalline characteristics of the NiCo<sub>2</sub>O<sub>4</sub> nanoparticles. Moreover, the more obviously monocrystal-like diffraction spots of the sample with SDS illustrate its higher crystallinity, which is well accordance with the XRD results.

Nitrogen sorption measurements are carried out to further study the surface physical structures (SSA, pore volume, average pore size and PSD) of as-synthesized NiCo<sub>2</sub>O<sub>4</sub> materials. Typical nitrogen adsorption–desorption isotherms, pore volume and PSD plots are shown in Fig. 4a–c respectively. Their nitrogen sorption isotherms exhibit type IV isotherms with H3 hysteresis loops, a characteristic of mesoporous materials. However, the hysteresis loop of the materials without SDS is extremely small and almost no plateau appears in the desorption branch, indicating the existence of large macropores [38]. The SSA, total pore volume, mesopore volume and average pore diameter of the SDS-assisted NiCo<sub>2</sub>O<sub>4</sub> materials are 88.63 m<sup>2</sup> g<sup>−1</sup>, 0.337 cm<sup>3</sup> g<sup>−1</sup>, 0.298 cm<sup>3</sup> g<sup>−1</sup> and 18.8 nm respectively in comparison with 88.94 m<sup>2</sup> g<sup>−1</sup>, 0.928 cm<sup>3</sup> g<sup>−1</sup>, 0.195 cm<sup>3</sup> g<sup>−1</sup> and 41 nm for the one without SDS (Table 1). Moreover, the pore size plots of the former exhibit a bimodal distribution at 7.8 and 17.5 nm compared to a trimodal distribution at 2.5, 5.6 and 31 nm of the latter (Table 1), indicating the superior mesoporous nanostructures of the SDS-assisted

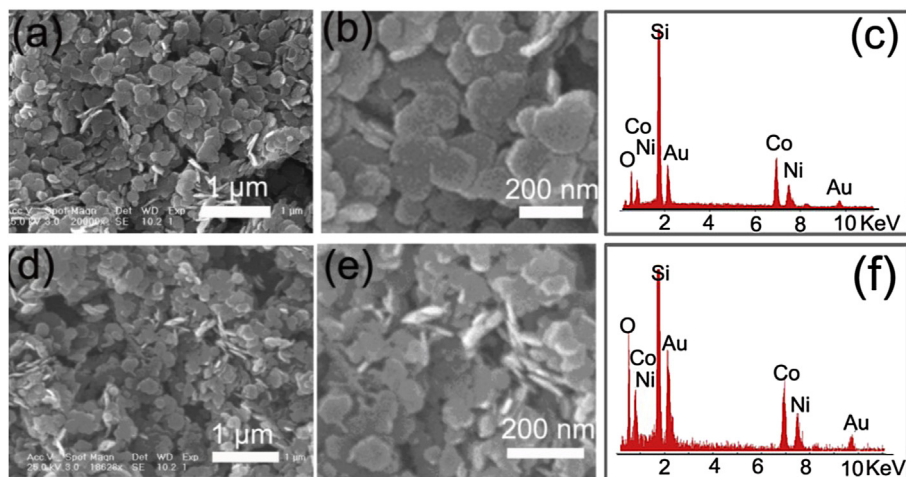
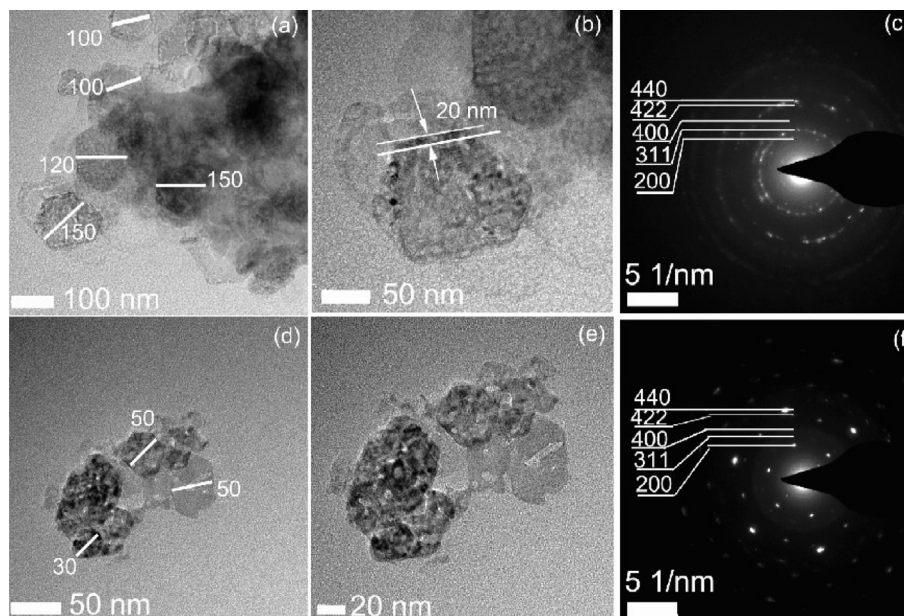


Fig. 2. SEM images and EDS patterns of NiCo<sub>2</sub>O<sub>4</sub> materials without (a–c) and with (d–e) SDS.





**Fig. 3.** TEM images of  $\text{NiCo}_2\text{O}_4$  materials without (a, b) and with (d, e) SDS and SAED patterns of  $\text{NiCo}_2\text{O}_4$  materials without (c) and with (f) SDS.

$\text{NiCo}_2\text{O}_4$  materials. Note that such superior mesoporous structures can ensure the penetration of electrolytes into the whole oxide matrix more facilely, which can further overcome the primary kinetic limits of electrochemical processes and therefore facilitate the electrochemical reactions [39,40]. It is also noted that templated mesoporous oxides possess accessible and uniform pores and much higher surface area and pore volume than conventional oxides, which make them attractive materials for adsorption and catalysis processes, especially those involving larger molecules [41]. Accordingly, the superior surface physical structures of the SDS-assistant  $\text{NiCo}_2\text{O}_4$  materials are of large benefit for MOR.

The surface chemical properties (chemical bonding states and compositions) of as-synthesized  $\text{NiCo}_2\text{O}_4$  materials were evaluated by XPS which are shown in Fig. 5. Typical signals of  $\text{O}_{1s}$ ,  $\text{Co}_{2p}$  and  $\text{Ni}_{2p}$  core levels are detected from the XPS. Of which, the  $\text{O}_{1s}$  spectra show four oxygen bonds (O1–O4) at 528.9, 530.0, 531.6, 533.0 eV (without SDS) and 529.2, 530.3, 531.4, 532.8 eV (with SDS), associating with the typical of metal–oxygen bonds [42], the oxygen in hydroxyl groups [43], the high number of defect sites with low

oxygen coordination in the material with small particle size [44], and the multiplicity of physis-/chemisorbed water at and within the surface [42], respectively. The  $\text{Co}_{2p}$  spectra of both samples consist of two spin-orbit doublets characteristics of  $\text{Co}^{2+}$  and  $\text{Co}^{3+}$  bonds and two shakeup satellites (identified as “Sat.”). Similarly, the  $\text{Ni}_{2p}$  spectra of both samples are composed of two spin-orbit doublets characteristics of  $\text{Ni}^{2+}$  and  $\text{Ni}^{3+}$  bonds and two shakeup satellites. These results show that the surfaces of both  $\text{NiCo}_2\text{O}_4$  materials have chemical compositions containing  $\text{Co}^{2+}$ ,  $\text{Co}^{3+}$ ,  $\text{Ni}^{2+}$  and  $\text{Ni}^{3+}$  species. Therefore, the formula of  $\text{NiCo}_2\text{O}_4$  can be generally expressed as follows:  $\text{Co}^{2+}_{1-x}\text{Co}^{3+}_x[\text{Co}^{3+}\text{Ni}^{2+}_x\text{Ni}^{3+}_{1-x}]\text{O}_4$  ( $0 < x < 1$ ) (the cations within the square bracket are in octahedral sites and the outside ones occupy the tetrahedral sites) [45]. Therefore, it is anticipated that the binary solid state redox couples  $\text{Co}^{3+}/\text{Co}^{2+}$  and  $\text{Ni}^{3+}/\text{Ni}^{2+}$  in the  $\text{NiCo}_2\text{O}_4$  structures can afford rich electroactive sites for  $\text{CH}_3\text{OH}$  electrooxidation, which may be one of the important factors contributing to the notable electrocatalytic performance of spinel  $\text{NiCo}_2\text{O}_4$  materials [46].

The quantitative information for surface Co and Ni active species of both  $\text{NiCo}_2\text{O}_4$  materials were also evaluated based on the XPS, and the results are shown in Table 2. It shows that the SDS-assisted  $\text{NiCo}_2\text{O}_4$  materials exhibit much higher (1.79 and 2.74 times respectively) surface intensities of Co and Ni species than those of the counterparts without SDS, but their surface Co/Ni ratio (1.08) is comparatively lower than that (1.65) of the one without SDS. Here, their differences in the surface chemical properties will largely influence their electrocatalytic performances, i.e. the higher surface

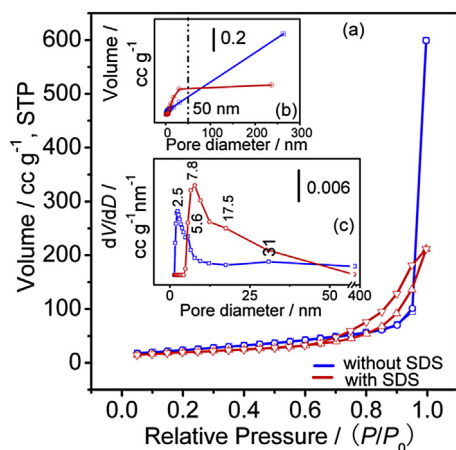


**Fig. 4.** Nitrogen adsorption/desorption isotherms (a), pore volume plots (b) and pore size distribution plots (c) of both  $\text{NiCo}_2\text{O}_4$  materials.

**Table 1**  
Nitrogen sorption data of both  $\text{NiCo}_2\text{O}_4$  materials.

$\text{NiCo}_2\text{O}_4$ materials	$S_{\text{BET}}^a$ ( $\text{m}^2 \text{g}^{-1}$ )	$V_{\text{T}}^b$ ( $\text{cm}^3 \text{g}^{-1}$ )	$V_{\text{meso}}^c$ ( $\text{cm}^3 \text{g}^{-1}$ )	$L_0^d$ (nm)	PSD <sup>e</sup> (nm)
Without SDS	88.94	0.928	0.195	41	2.5, 5.6, 31
With SDS	86.63	0.337	0.298	18.8	7.8, 17.5

<sup>a</sup> BET surface area ( $\text{m}^2 \text{g}^{-1}$ ).

<sup>b</sup> Total pore volume ( $\text{cm}^3 \text{g}^{-1}$ ).

<sup>c</sup> Mesopore volume ( $\text{cm}^3 \text{g}^{-1}$ ).

<sup>d</sup> Average pore diameter (nm).

<sup>e</sup> Pore size distribution (nm).

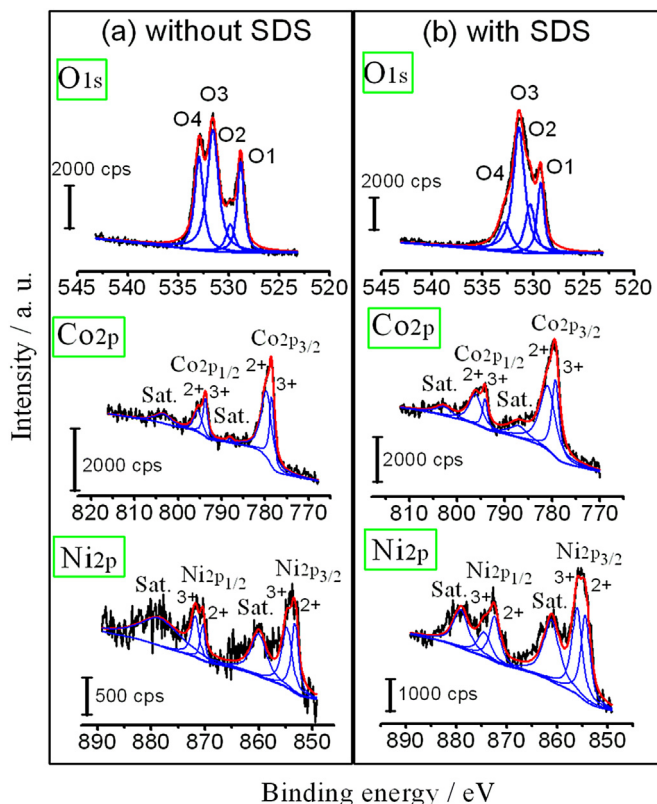


Fig. 5. XPS profiles ( $O_{1s}$ ,  $Co_{2p}$  and  $Ni_{2p}$  core levels) of  $NiCo_2O_4$  materials without (a) and with (b) SDS.

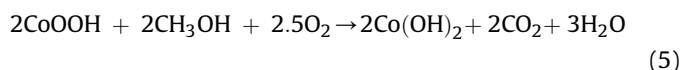
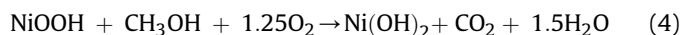
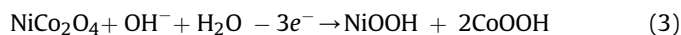
content of Co and Ni species will contribute to the more electroactive sites, whereas the higher extent surface non-stoichiometry (lattice defect sites) of Co/Ni ratio may cause the inferior structural stability.

Based on the above investigations, one can see that the SDS soft template plays a dominant role in the hydrothermal synthesis of mesoporous  $NiCo_2O_4$  nanomaterials and it highly affects their physicochemical properties. Firstly, the SDS can promote the formation of superior mesoporous nanostructures. The SDS (chemical formula:  $C_{12}H_{25}SO_4-Na^+$ ) is a typical anionic surfactant, which can act as the structure-directing agent in the fabrication of mesoporous  $NiCo_2O_4$  nanoparticles through interface self-assembly processes via a quasi-reverse micelle mechanism (Scheme S1, Supporting information). Secondly, the SDS can effectively restrain the growth of ultimate  $NiCo_2O_4$  crystals because of the enclosure of micelles during the hydrothermal process formed by the SDS template, resulting in the smaller and thinner particle size, and this may comparatively enhance the surface intensities of elements versus those in the bulk. Thirdly, the surroundings of the micelles tend to be more beneficial to the formation monocrystal-like structures, leading to the higher crystallinity of  $NiCo_2O_4$  particles.

### 3.2. $CH_3OH$ electrooxidation behavior of the $NiCo_2O_4$ electrode

The methanol electrooxidation behavior on the SDS-assisted  $NiCo_2O_4$  electrode was examined by CV, LSV, CA and EIS tests, and the  $NiCo_2O_4$  electrode without SDS was also tested for comparison. Fig. 6a shows the CV plots of these two electrodes in 1 M KOH blank electrolytes at a scan rate of  $10\text{ mV s}^{-1}$ . As shown in the figure, both  $NiCo_2O_4$  electrodes present one pair of redox peaks centering at about 0.51 V/0.25 V, which originates from the overall

charge transfer processes of solid state redox couples  $Co^{3+}/Co^{2+}$  ( $CoOOH/Co_3O_4$ ) and  $Ni^{3+}/Ni^{2+}$  ( $NiOOH/NiO$ ) [47,48], nicely reflecting the richer redox chemistry feature of spinel  $NiCo_2O_4$ , which may supply sufficient electroactive centers for methanol electrooxidation. Note that the SDS-assisted  $NiCo_2O_4$  electrode exhibits much stronger redox peaks (A, C) than those (A', C') of the one without SDS, suggesting much higher electrochemical activity. Fig. 6b depicts the CV plots of these two electrodes in 1 M KOH with 0.5 M  $CH_3OH$  electrolytes at a scan rate of  $10\text{ mV s}^{-1}$ . As can be seen in the figure, a much higher anodic current is observed on the SDS-assisted  $NiCo_2O_4$  electrode compared to the current without SDS, indicating much higher catalytic activity for  $CH_3OH$  electrooxidation. The corresponding catalytic mechanism on the  $NiCo_2O_4$  electrode, which is supposed to be similar to that on the  $NiO$  and  $Co_3O_4$  electrodes, can be briefly described as follows [18,49,50]:



Current density is one of the important parameters for evaluating the catalysts. As shown in Fig. 6b, the maximum current density can reach  $125\text{ mA cm}^{-2}$  at 0.6 V (vs. Hg/HgO) for the SDS-assisted  $NiCo_2O_4$  electrode, comparing with  $93\text{ mA cm}^{-2}$  for the one without SDS, which mainly originated from higher surface content of Co and Ni active species and better mesoporous nanostructures of the SDS-assisted  $NiCo_2O_4$  materials. The onset potential is another important parameter for catalysts. From Fig. 6c and d, one can see that the onset potentials for methanol oxidation on the  $NiCo_2O_4$  electrodes are all around 0.37 V, similar to the starting potential for the co-transition of Ni and Co redox reactions, which is much lower than that for the reported  $Co_3O_4$  electrodes (0.49–0.57 V) [21,34,35] and  $NiO$  electrodes (0.49–0.5 V) [34,35], demonstrating the notable synergistic function of Co and Ni species for the boost of catalytic activity towards methanol electrooxidation.

Remarkably, the catalytic activity of as-synthesized  $NiCo_2O_4$  electrodes is superior to many reported Pt-free electrocatalysts for methanol electrooxidation in alkaline media (Table S1, Supporting information). For example, the  $NiCo_2O_4$  electrode with SDS is better than  $Co_3O_4$  [21,34,35],  $NiO$  [18,34,35],  $NiO/CNTs$  composites [19], nickel foam supported porous  $Co_3O_4/NiO$  core/shell nanowire array electrode [21] as well as  $NiCo_2O_4$  electrodes [33–35].

Herein, the maximum activity for MOR in alkaline media as for the state-of-art low-Pt and Pt-free catalysts was also examined and compared with the values in acidic condition. As can be seen from Table S2 and Fig. S1, the characterized low-Pt catalysts can be classified into three distinct regions with the boundaries of  $0.25\text{ mA } \mu\text{g}^{-1}\text{ Pt}$ ,  $1\text{ mA } \mu\text{g}^{-1}\text{ Pt}$  and  $10\text{ mA } \mu\text{g}^{-1}\text{ Pt}$ . It is demonstrated that most of the examined electrocatalysts [51,52] present intermediate electrocatalytic activity ( $0.25\text{--}1\text{ mA } \mu\text{g}^{-1}\text{ Pt}$ ), while a few catalysts [53,54] present lower activity ( $<0.25\text{ mA } \mu\text{g}^{-1}\text{ Pt}$ ). Also, only a few catalysts [52] exhibit a higher activity ( $1\text{--}10\text{ mA } \mu\text{g}^{-1}\text{ Pt}$ ). The above phenomenon is rather similar to that in the acidic media for MOR, but the maximum activity in alkaline media as for the low-Pt catalysts seems to be smaller than that in acidic media. For example, the characterized  $Pt_2Au_1Sn_1/CNT$  catalyst exhibited the largest value of  $1.7\text{ mA } \mu\text{g}^{-1}\text{ Pt}$  at 0.2 V (vs. Hg/HgO), which is much lower than that of the highest core-shell  $CdSe@Pt$  nanocomposites ( $7.13\text{ mA } \mu\text{g}^{-1}\text{ Pt}$  at 0.8 V vs. Hg/HgO) in acidic media [55]. Based on the Table S3 and Fig. S2, one can see that most of the characterized

**Table 2**  
XPS quantitative data for surface Co and Ni elements of both NiCo<sub>2</sub>O<sub>4</sub> materials.

Intensity ratio (with SDS/without SDS)		Atomic ratio (Co <sub>2p</sub> /Ni <sub>2p</sub> )	
Co <sub>2p</sub>	Ni <sub>2p</sub>	Without SDS	With SDS
1.79	2.74	1.65	1.08

Pt-free catalysts exhibited a high activity in the alkaline media, which is different from the reported phenomenon in the acidic media that usually displayed a small activity [56]. Herein, the maximum current density of examined Pt-free catalysts in alkaline medium is ascribed to NiCu/GC electrode [57], which exhibits the peak current density of 300 mA cm<sup>-2</sup> at 0.7 V vs. Hg/HgO in 1 M KOH and 0.7 M CH<sub>3</sub>OH solutions. The value is far bigger than the reported Pd/TiO<sub>x</sub> nanotube with 20 mA cm<sup>-2</sup> at 0.7 V vs. SCE in 1 M H<sub>2</sub>SO<sub>4</sub> and 1 M CH<sub>3</sub>OH solutions [58].

The influence of CH<sub>3</sub>OH concentration on the efficiency of the NiCo<sub>2</sub>O<sub>4</sub> electrocatalysts towards MOR was investigated by the steady-state polarization method. Fig. 7 depicts the measured polarization curves in 1 M KOH and x M CH<sub>3</sub>OH solutions with x from 0.3 to 0.9 at a scan rate of 1 mV s<sup>-1</sup>. Obviously, higher CH<sub>3</sub>OH concentration produced larger MOR current density. For the NiCo<sub>2</sub>O<sub>4</sub> without SDS, the current density at 0.6 V increased from 60 to 86 mA cm<sup>-2</sup> when the CH<sub>3</sub>OH concentration increased from 0.3 to 0.9 M. The NiCo<sub>2</sub>O<sub>4</sub> with SDS shows a smaller current increment along with the climbing of CH<sub>3</sub>OH concentration, exhibiting the value from 95 to 114 mA cm<sup>-2</sup>. The relationship between log *j* at 0.6 V and log C<sub>CH<sub>3</sub>OH</sub> for the NiCo<sub>2</sub>O<sub>4</sub> without and with SDS was plotted in the insets of Fig. 7a and b respectively. As can be seen from these figures, a close linear relationship was observed. The slope of the plots, which is defined as the reaction order (*P*) of the MOR with respect to CH<sub>3</sub>OH, was found to be 0.33 and 0.17 for the NiCo<sub>2</sub>O<sub>4</sub> without and with SDS respectively, which might be highly related with their different surface physicochemical properties.

The stability of catalysts is also an important factor for being evaluated. Fig. 8a depicts the CA tests of these two electrodes at 0.6 V (vs. Hg/HgO) for consecutive 1000 s, it shows that the SDS-assisted NiCo<sub>2</sub>O<sub>4</sub> electrode possesses 72% current retention, which is lightly lower than the one without SDS (75%). The stability of both NiCo<sub>2</sub>O<sub>4</sub> electrodes was also examined by CV cycling tests. As shown in Fig. 8b, the current density for the SDS-assisted NiCo<sub>2</sub>O<sub>4</sub> electrode at 0.6 V (vs. Hg/HgO) exhibits 71% retention after 1000 cycles at 30 mV s<sup>-1</sup>, comparing with 73% retention for the one without SDS, which corresponds well with the CA tests. Here, the lightly inferior cycling stability of the SDS-assisted NiCo<sub>2</sub>O<sub>4</sub> electrode may be due to the higher extent surface non-stoichiometry (lattice defect) of Co/Ni ratio in the materials, which may be responsible for the lightly lower structural stability.

Herein, the methanol electrooxidation performance of the NiCo<sub>2</sub>O<sub>4</sub> electrode (with SDS) was also compared with that of commercial Pt/C catalyst (Fig. S3, Supporting information). It shows that the onset potential and peak current density of the Pt/C catalyst are about -0.4 V (vs. Hg/HgO) and 306 mA cm<sup>-2</sup> (at 0.14 V), which are superior to those (0.37 V; 125 mA cm<sup>-2</sup> at 0.6 V) of NiCo<sub>2</sub>O<sub>4</sub> electrode with SDS. This is a common phenomenon in all metal oxides/hydroxides catalysts for alkaline DMFCs [21]. So there is still large scope for improvement of the electrocatalytic performance of metal oxides based electrocatalysts for methanol electrooxidation. However, the Pt/C catalyst exhibited relatively worse electrochemical stability (52.8% current retention after 600 s) for MOR compared with the NiCo<sub>2</sub>O<sub>4</sub> electrode with SDS (72.3% retention). Moreover, a serious current decay (from 246 to 138 mA cm<sup>-2</sup>) is observed for the Pt/C catalyst in the first 20 s, whereas the NiCo<sub>2</sub>O<sub>4</sub> electrode exhibited a smaller decay (from 137 to 115 mA cm<sup>-2</sup>) during the first 20 s, indicating the superior anti-poison characteristics of the NiCo<sub>2</sub>O<sub>4</sub> electrode. Based on the above analysis, a combination of Pt/C and NiCo<sub>2</sub>O<sub>4</sub> components, i.e. the development of NiCo<sub>2</sub>O<sub>4</sub>-Pt/C composite catalysts, may be an effective way to simultaneously achieve the low overpotential, high

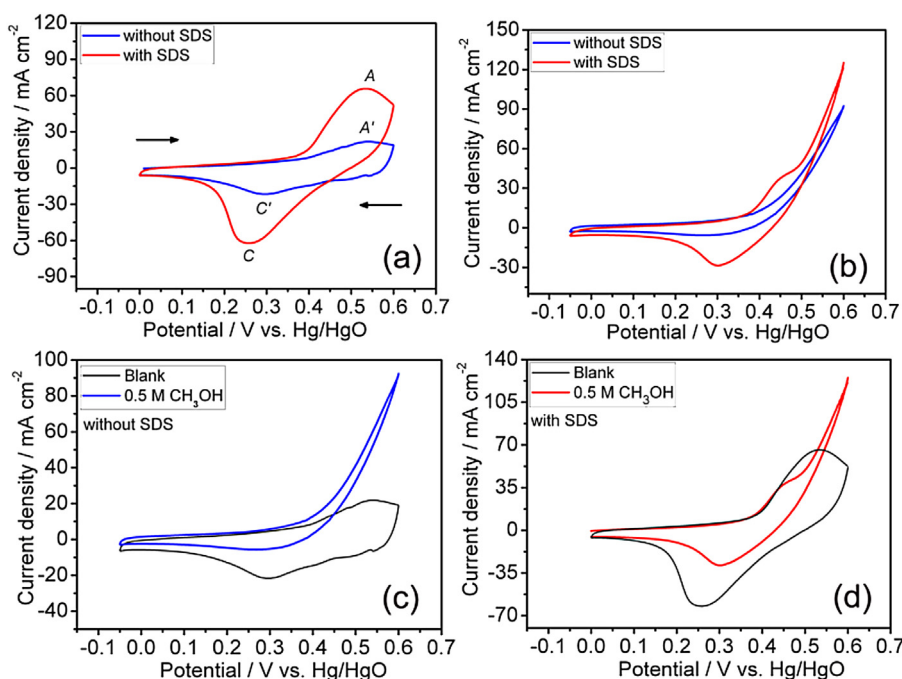


**Fig. 6.** CV plots at 10 mV s<sup>-1</sup> in 1 M KOH electrolytes (a) and CV plots at 10 mV s<sup>-1</sup> in 1 M KOH electrolytes with 0.5 M CH<sub>3</sub>OH (b) of both NiCo<sub>2</sub>O<sub>4</sub> electrodes; CV plots at 10 mV s<sup>-1</sup> in 1 M KOH electrolytes in absence and presence of 0.5 M CH<sub>3</sub>OH for the NiCo<sub>2</sub>O<sub>4</sub> electrode without (c) and with (d) SDS.



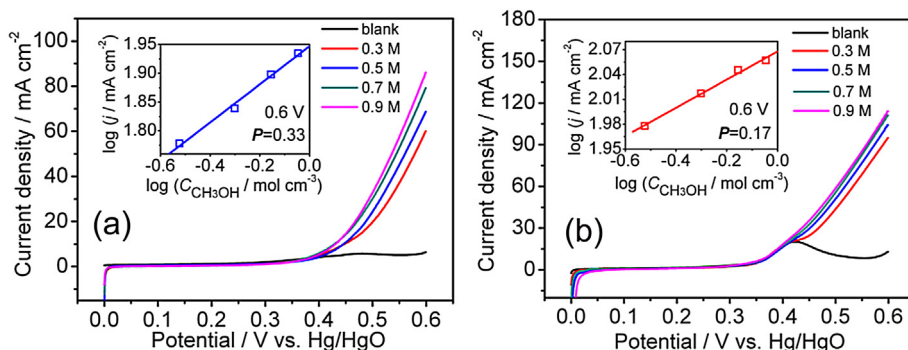


**Fig. 7.** Steady-state polarization curves for the MOR on  $\text{NiCo}_2\text{O}_4$  electrodes without SDS (a) and with SDS (b) at different concentrations of  $\text{CH}_3\text{OH}$  at a scan rate of  $1 \text{ mV s}^{-1}$  (Insets show the plots of  $\log j$  versus  $\log C_{\text{CH}_3\text{OH}}$ ).

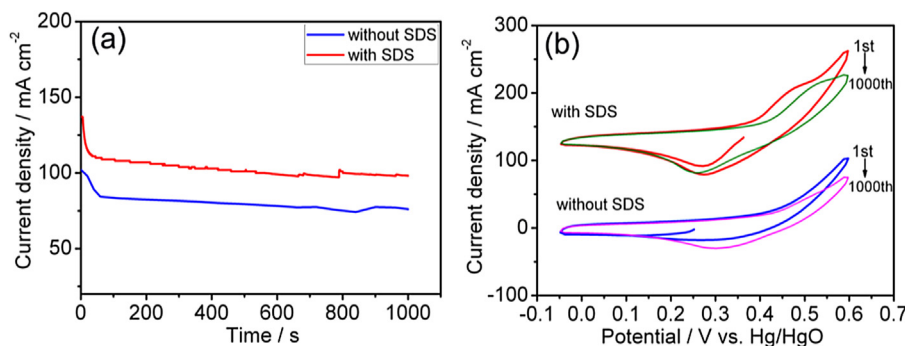


**Fig. 8.** CA curves at 0.6 V in 1 M KOH with 0.5 M  $\text{CH}_3\text{OH}$  electrolytes (a) and CV plots for the first and the 1000th cycles at  $30 \text{ mV s}^{-1}$  in 1 M KOH electrolytes with 0.5 M  $\text{CH}_3\text{OH}$  (b) of both  $\text{NiCo}_2\text{O}_4$  electrodes.

current density, desirable electrochemical stability and superior anti-poison property for MOR.

The conductivity of both  $\text{NiCo}_2\text{O}_4$  electrodes were also examined using EIS technique measured both at a fixed frequency of 100,000 Hz and in the frequency region of 100,000 Hz–0.01 Hz, and the results are shown in Fig. 9a and b. As can be seen that, the  $\text{NiCo}_2\text{O}_4$  electrode with SDS shows approximately 5 times higher conductivity ( $0.035 \text{ S cm}^{-1}$ ) than the one without SDS ( $0.0074 \text{ S cm}^{-1}$ ), and this might be owing to the higher extent surface non-stoichiometry (i.e. lattice defect sites) of Co/Ni ratio in the  $\text{NiCo}_2\text{O}_4$  lattice that makes the electron hopping process more easily [59,60], which may largely accelerate the interfacial electron transportation process for methanol catalytic reactions.

Since the charge transfer resistance ( $R_{\text{ct}}$ ) and the knee frequency ( $f_{\text{knee}}$ ) are very important parameters for evaluating the

electrocatalytic activity of a catalyst, and thus EIS tests for both  $\text{NiCo}_2\text{O}_4$  electrodes were all recorded in 1 M KOH blank and 0.5 M  $\text{CH}_3\text{OH}$  electrolytes. The Nyquist plots and admittance plots of experimental and fitting data are shown in Fig. 10a–d. The higher and lower frequency regions of the measured impedance spectra are just divided by the “knee” or “onset” frequency ( $f_{\text{knee}}$ ), the charge saturation point of the electrode, which describes the lower limit of the high frequency region (charge transfer process) and is a measure of the electrochemical response of the electrode. The measured impedance spectra were simulated on the basis of the proposed equivalent circuits, which are given in the insets of Fig. 10a and c. These model circuits consist of six elements: the inductance ( $L$ ), the equivalent series resistance or the ohmic resistance ( $R_e$ ), the constant phase element (CPE) ( $Q$ ), the charge-transfer resistance ( $R_{\text{ct}}$ ), the Warburg impedance ( $W$ ), and the

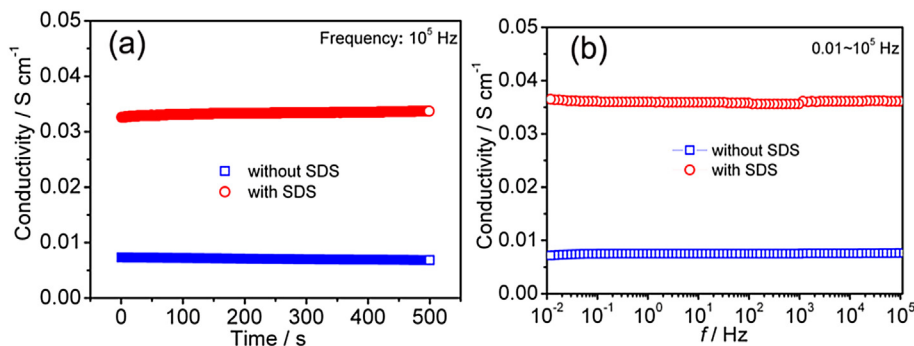


**Fig. 9.** Conductivity profiles as function of time at a fixed frequency of 100,000 Hz (a) and the plots of conductivity against frequency (b) of both  $\text{NiCo}_2\text{O}_4$  electrodes.

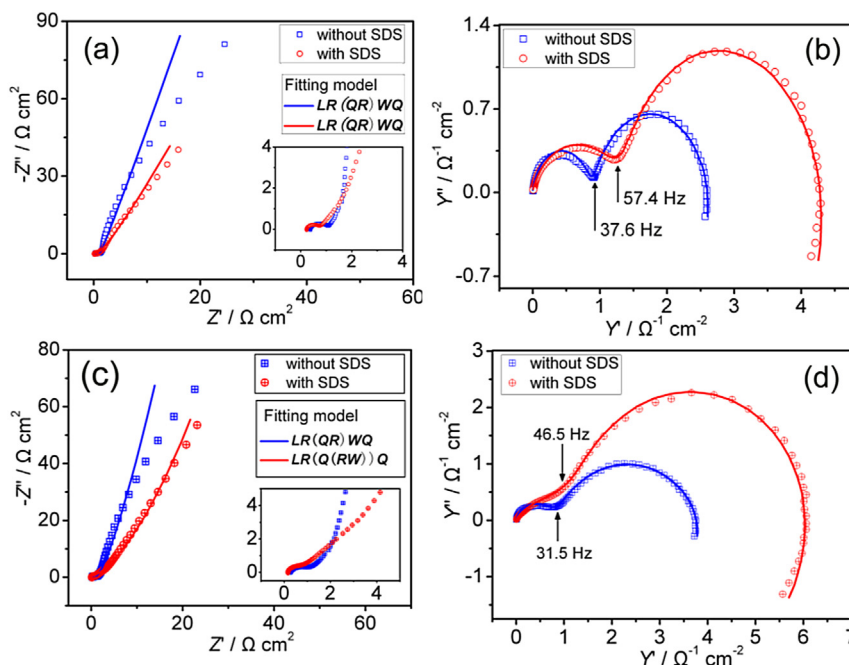


**Fig. 10.** Nyquist plots (a) and admittance plots (b) in 1 M KOH electrolytes, and Nyquist plots (c) and admittance plots (d) in 1 M KOH electrolytes with 0.5 M CH<sub>3</sub>OH of both NiCo<sub>2</sub>O<sub>4</sub> electrodes (Inset shows the enlarged parts in the high frequency regions and fitting models, hollow symbols and solid lines represent the experimental and fitting data respectively).

limit capacitance ( $C_i$ ) [61]. The CPE ( $Q$ ) is used in place of double-layer capacitance ( $C_{dl}$ ) at the electrode/electrolyte boundary, indicating the deviation from the ideal behavior of a perfect capacitor. The impedance of CPE is defined as the following equation [62]:

$$Z_{CPE} = [(Y_0 j\omega)^n]^{-1} \quad (6)$$

where  $Y_0$  is the frequency-independent constant relating to the surface electroactive properties,  $\omega$  is the radial frequency, the exponent  $n$  arises from the slope of  $\log Z$  vs.  $\log f$  and has values  $-1 \leq n \leq 1$ . If  $n = 0$ , the CPE behaves as a pure resistor;  $n = 1$ , CPE behaves as a pure capacitor,  $n = -1$ , CPE behaves as an inductor; while  $n = 0.5$  corresponds to Warburg impedance which is associated with the domain of mass transport control arising from the diffusion of ions to and from the electrode/electrolytes interface.

The fitted values of impedimetric parameters are presented in Table 3. As can be seen in the table, in the absence of CH<sub>3</sub>OH, the SDS-assisted NiCo<sub>2</sub>O<sub>4</sub> electrode exhibits smaller  $R_{ct}$  and larger  $f_{knee}$  values (0.46  $\Omega \text{ cm}^2$ , 57.4 Hz) compared with those (0.72  $\Omega \text{ cm}^2$ , 37.6 Hz) of the NiCo<sub>2</sub>O<sub>4</sub> electrode without SDS, demonstrating the faster charge transfer rate and better electrochemical response of the SDS-assisted NiCo<sub>2</sub>O<sub>4</sub> electrode which would be contributable to the higher catalytic activity towards methanol electrooxidation. In the presence of CH<sub>3</sub>OH, the SDS-assisted NiCo<sub>2</sub>O<sub>4</sub> electrode still

exhibits smaller  $R_{ct}$  and larger  $f_{knee}$  values (0.49  $\Omega \text{ cm}^2$ , 46.5 Hz) compared with those (0.80  $\Omega \text{ cm}^2$ , 31.5 Hz) for the one without SDS, indicating the higher catalytic activity towards methanol electrooxidation. Note that, before and after addition of CH<sub>3</sub>OH, the  $R_{ct}$  and  $f_{knee}$  values of both NiCo<sub>2</sub>O<sub>4</sub> electrodes only slightly changed, demonstrating that the binary spinel NiCo<sub>2</sub>O<sub>4</sub> electrode has a high tolerance to intermediate poisoning, which is superior to the reported Co<sub>3</sub>O<sub>4</sub> and NiO electrodes that may be poisoned by the adsorption of methanol or the oxidation intermediates on the electrode [34,35]. In all, the above results well demonstrate the superiority of the SDS-assisted NiCo<sub>2</sub>O<sub>4</sub> electrode in the catalysis of methanol electrooxidation.

Steady-state polarization curves of methanol electrooxidation on both NiCo<sub>2</sub>O<sub>4</sub> electrodes were measured to further evaluate their catalytic activity. Fig. 11 shows the LSV curves and corresponding Tafel plots (inset). The polarization curves were recorded in 1 M KOH and 0.5 M CH<sub>3</sub>OH electrolytes at a scan rate of 1 mV s<sup>-1</sup>. It can be seen that the NiCo<sub>2</sub>O<sub>4</sub> electrode with SDS exhibits an obviously higher MOR catalytic performance with a current density of 104 mA cm<sup>-2</sup> at 0.6 V compared with the value of 69 mA cm<sup>-2</sup> for the NiCo<sub>2</sub>O<sub>4</sub> electrode without SDS. Tafel plots in strong polarization regions (0.35–0.45 V) were used to obtain Tafel slopes ( $b$ ) and exchange current densities ( $j^0$ ) of both electrodes. As can be found that, the Tafel slope and exchange current density for the NiCo<sub>2</sub>O<sub>4</sub> electrode with SDS are around 103 mV dec<sup>-1</sup> and  $8.9 \times 10^{-6} \text{ A cm}^{-2}$  in comparison with 138 mV dec<sup>-1</sup> and  $7.1 \times 10^{-6} \text{ A cm}^{-2}$  for the one

**Table 3**

The fitting values of impedimetric parameters for both NiCo<sub>2</sub>O<sub>4</sub> electrodes in 1 M KOH electrolytes in absence and presence of 0.5 M CH<sub>3</sub>OH.

	Impedimetric parameters									
	$L$ (H cm <sup>2</sup> )	$R_e$ ( $\Omega \text{ cm}^2$ )	$Q1$ , $Y_0$ ( $\Omega^{-1} \text{ s}^n \text{ cm}^{-2}$ )	$R_{ct}$ ( $\Omega \text{ cm}^2$ )	$W$ , $Y_0$ ( $\Omega^{-1} \text{ s}^{0.5} \text{ cm}^{-2}$ )	$Q2$ , $Y_0$ ( $\Omega^{-1} \text{ s}^n \text{ cm}^{-2}$ )	$n1$	$n2$	$f_{knee}$ (Hz)	$\chi^2$ (E-3)
A-without SDS	7.2E-8	0.38	1.5E-3	0.72	1.10	0.11	0.82	0.90	37.6	1.36
P-without SDS	5.2E-8	0.26	4.9E-3	0.80	0.33	0.16	0.75	0.94	31.5	1.43
A-with SDS	6.4E-8	0.23	1.8E-3	0.46	0.39	0.22	0.86	0.87	57.4	0.78
P-with SDS	6.9E-8	0.17	1.2E-3	0.49	0.12	0.30	0.98	0.98	46.5	0.62

Note: The symbols "A" and "P" represent the 1 M KOH electrolytes in absence and presence of 0.5 M CH<sub>3</sub>OH respectively.



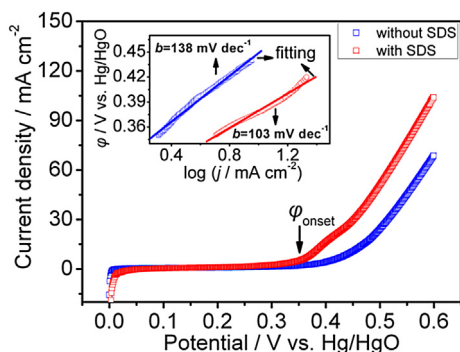


**Fig. 11.** Steady-state polarization curves for the MOR on both  $\text{NiCo}_2\text{O}_4$  electrodes in 1 M KOH and 0.5 M  $\text{CH}_3\text{OH}$  electrolytes at a scan rate of  $1 \text{ mV s}^{-1}$  (Insets show the corresponding Tafel plots).

without SDS, suggesting that the  $\text{NiCo}_2\text{O}_4$  electrode with SDS possesses faster electrochemical kinetics for MOR.

#### 4. Conclusions

A facile SDS-assistant hydrothermal method was employed to fabricate mesoporous  $\text{NiCo}_2\text{O}_4$  nanoparticles, which exhibit the superior mesoporous nanostructure with a specific surface area and mesopore volume of  $88.63 \text{ m}^2 \text{ g}^{-1}$  and  $0.298 \text{ cm}^3 \text{ g}^{-1}$ . Impressively, the SDS-assisted  $\text{NiCo}_2\text{O}_4$  materials show much better electrocatalytic activity for  $\text{CH}_3\text{OH}$  electrooxidation than the counterparts without SDS assistance. A current density of  $125 \text{ mA cm}^{-2}$  and 72% current retention for consecutive 1000 s were achieved for the SDS-assisted  $\text{NiCo}_2\text{O}_4$  electrode at 0.6 V in 1 M KOH and 0.5 M  $\text{CH}_3\text{OH}$  electrolytes. The desirable electrocatalytic capability of the SDS-assisted  $\text{NiCo}_2\text{O}_4$  materials is mainly owing to their richer surface electroactive sites of Co and Ni species and superior mesoporous nanostructures, leading to the enhanced electrocatalytic activity and faster electrochemical kinetics, which are very promising for further promotion of Pt-free catalysts based alkaline DMFCs.

#### Acknowledgments

This research was supported by Scientific Research Foundation for the Returned Overseas Chinese Scholars and State Education Ministry (SRF for ROCS, SEM) and Hundred Talents Program of Chinese Academy of Sciences.

#### Appendix A. Supplementary data

Supplementary data related to this article can be found at <http://dx.doi.org/10.1016/j.jpowsour.2013.11.063>.

#### References

- [1] A.S. Arico, P. Bruce, B. Scrosati, J.M. Tarascon, W. Van Schalkwijk, *Nat. Mater.* 4 (2005) 366–377.
- [2] C. Liu, F. Li, L.P. Ma, H.M. Cheng, *Adv. Mater.* 22 (2010) E28–E62.
- [3] Y. Lu, J.P. Tu, C.D. Gu, X.H. Xia, X.L. Wang, S.X. Mao, *J. Mater. Chem.* 21 (2011) 4843–4849.
- [4] Y.S. Li, T.S. Zhao, Z.X. Liang, *J. Power Sources* 190 (2009) 223–229.
- [5] Z.L. Liu, X.Y. Ling, X.D. Su, J.Y. Lee, *J. Phys. Chem. B* 108 (2004) 8234–8240.
- [6] J.H. Jiang, T. Aulich, *J. Power Sources* 209 (2012) 189–194.
- [7] L.X. Ding, G.R. Li, Z.L. Wang, Z.Q. Liu, H. Liu, Y.X. Tong, *Chem. Eur. J.* 18 (2012) 8386–8391.
- [8] S. Mayavan, H.-S. Jang, M.-J. Lee, S.H. Choi, S.-M. Choi, *J. Mater. Chem. A* 1 (2013) 3489–3494.
- [9] S.S. Mahapatra, A. Dutta, J. Datta, *Int. J. Hydrogen Energy* 36 (2011) 14873–14883.
- [10] H.H. Wang, Z.H. Sun, Y. Yang, D.S. Su, *Nanoscale* 5 (2013) 139–142.
- [11] C. Bianchini, P.K. Shen, *Chem. Rev.* 109 (2009) 4183–4206.
- [12] H.J. Huang, X. Wang, *J. Mater. Chem.* 22 (2012) 22533–22541.
- [13] H.P. Liu, J.Q. Ye, C.W. Xu, S.P. Jiang, Y.X. Tong, *J. Power Sources* 177 (2008) 67–70.
- [14] J. Kua, W.A. Goddard, *J. Am. Chem. Soc.* 121 (1999) 10928–10941.
- [15] B.Y. Xia, H.B. Wu, X. Wang, X.W. Lou, *J. Am. Chem. Soc.* 134 (2012) 13934–13937.
- [16] J.F. Xu, X.Y. Liu, Y. Chen, Y.M. Zhou, T.H. Lu, Y.W. Tang, *J. Mater. Chem.* 22 (2012) 23659–23667.
- [17] J.H. Yuan, B. He, L.J. Hong, J. Lu, J.G. Miao, L. Niu, *J. Mater. Chem.* 22 (2012) 19658–19665.
- [18] N. Spinner, W.E. Mustain, *Electrochim. Acta* 56 (2011) 5656–5666.
- [19] X.L. Tong, Y. Qin, X.Y. Guo, O. Moutanabbir, X.Y. Ao, E. Pippel, L.B. Zhang, M. Knez, *Small* 8 (2012) 3390–3395.
- [20] R.S. Amin, R.M.A. Hameed, K.M. El-Khatib, M.E. Youssef, A.A. Elzatahy, *Electrochim. Acta* 59 (2012) 499–508.
- [21] J.B. Wu, Z.G. Li, X.H. Huang, Y. Lin, *J. Power Sources* 224 (2013) 1–5.
- [22] Y.C. Zhao, S.L. Nie, H.W. Wang, J.N. Tian, Z. Ning, X.X. Li, *J. Power Sources* 218 (2012) 320–330.
- [23] B.K. Boggs, G.G. Botte, *Electrochim. Acta* 55 (2010) 5287–5293.
- [24] D.D. Zhao, W.J. Zhou, H.L. Li, *Chem. Mater.* 19 (2007) 3882–3891.
- [25] G.Y. Zhang, B. Guo, J. Chen, *Sens. Actuators B: Chem.* 114 (2006) 402–409.
- [26] B. Cui, H. Lin, J.B. Li, X. Li, J. Yang, J. Tao, *Adv. Funct. Mater.* 18 (2008) 1440–1447.
- [27] Y.G. Li, P. Hasin, Y.Y. Wu, *Adv. Mater.* 22 (2010) 1926–1929.
- [28] R. Boggio, A. Carugati, G. Lodi, S. Trasatti, *J. Appl. Electrochem.* 15 (1985) 335–349.
- [29] B. Chi, J.B. Li, Y.S. Han, Y.J. Chen, *Int. J. Hydrogen Energy* 29 (2004) 605–610.
- [30] R.N. Singh, J.F. Koenig, G. Poillerat, P. Chartier, *J. Electroanal. Chem.* 314 (1991) 241–257.
- [31] Z.Q. Liu, Q.Z. Xu, J.Y. Wang, N. Li, S.H. Guo, Y.Z. Su, H.J. Wang, J.H. Zhang, S. Chen, *Int. J. Hydrogen Energy* 38 (2013) 6657–6662.
- [32] Y.Y. Gao, D.X. Cao, G.L. Wang, C.L. Yin, *Acta Phys. Chim. Sin.* 26 (2010) 29–33.
- [33] R. Ding, L. Qi, M.J. Jia, H.Y. Wang, *Catal. Sci. Technol.* 3 (2013) 3207–3215.
- [34] R. Ding, L. Qi, M.J. Jia, H.Y. Wang, *Electrochim. Acta* 113 (2013) 290–301.
- [35] L. Qian, L. Gu, L. Yang, H.Y. Yuan, D. Xiao, *Nanoscale* 5 (2013) 7388–7396.
- [36] M.U. Anu Prathap, R. Srivastava, *Nano. Energy* 2 (2013) 1046–1053.
- [37] R. Ding, L. Qi, M.J. Jia, H.Y. Wang, *J. Appl. Electrochem.* 43 (2013) 903–910.
- [38] Y.T. Wang, A.H. Lu, H.L. Zhang, W.C. Li, *J. Phys. Chem. C* 115 (2011) 5413–5421.
- [39] D.W. Wang, F. Li, M. Liu, G.Q. Lu, H.M. Cheng, *Angew. Chem. Int. Ed.* 47 (2008) 373–376.
- [40] K.H. Chang, C.C. Hu, C.Y. Chou, *Chem. Mater.* 19 (2007) 2112–2119.
- [41] S.M. Morris, J.A. Horton, M. Jaroniec, *Microporous Mesoporous Mater.* 128 (2010) 180–186.
- [42] J.F. Marco, J.R. Gancedo, M. Gracia, *J. Solid State Chem.* 153 (2000) 74–81.
- [43] Y.E. Roginskaya, O.V. Morozova, E.N. Lubnin, Y.E. Ulitina, G.V. Lopukhova, S. Trasatti, *Langmuir* 13 (1997) 4621–4627.
- [44] V.M. Jimenez, A. Fernandez, J.P. Espinos, A.R. Gonzalez-Elipe, *J. Electron Spectrosc. Relat. Phenom.* 71 (1995) 61–71.
- [45] J.G. Kim, D.L. Pugmire, D. Battaglia, M.A. Langell, *Appl. Surf. Sci.* 165 (2000) 70–84.
- [46] B. Cui, H. Lin, Y.Z. Liu, J.B. Li, P. Sun, X.C. Zhao, C.J. Liu, *J. Phys. Chem. C* 113 (2009) 14083–14087.
- [47] R. Ding, L. Qi, H.Y. Wang, *J. Solid State Electrochim.* 16 (2012) 3621–3633.
- [48] R. Ding, L. Qi, M.J. Jia, H.Y. Wang, *Electrochim. Acta* 107 (2013) 494–502.
- [49] H. Heli, H. Yadegari, *Electrochim. Acta* 55 (2010) 2139–2148.
- [50] M. Asgari, M.G. Maragheh, R. Davarkhah, E. Lohrasbi, *J. Electrochem. Soc.* 158 (2011) K225–K229.
- [51] P. Justin, G. Ranga Rao, *Catal. Today* 141 (2009) 138–143.
- [52] M. Roca-Ayats, G. Garcia, J.L. Galante, Miguel A. Peña, M.V. Martínez-Huerta, *J. Phys. Chem. C* 117 (2013) 20769–20777.
- [53] H.M. Zhang, W.Q. Zhou, Y.K. Du, P. Yang, C.Y. Wan, J.K. Xu, *Int. J. Hydrogen Energy* 35 (2010) 13290–13297.
- [54] B. Singh, L. Murad, F. Laffir, C. Dickinson, E. Dempsey, *Nanoscale* 3 (2011) 3334–3349.
- [55] J. Yang, X. Chen, F. Ye, C. Wang, Y. Zheng, J. Yang, *J. Mater. Chem.* 21 (2011) 9088–9094.
- [56] A. Brouzgou, S.Q. Song, P. Tsiakaras, *Appl. Catal. B: Environ.* 127 (2012) 371–388.
- [57] I. Danaee, M. Jafarian, F. Forouzandeh, F. Goba, M.G. Mahjani, *Int. J. Hydrogen Energy* 34 (2009) 859–869.
- [58] M. Wang, D.-J. Guo, H.-L. Li, *J. Solid State Chem.* 178 (2005) 1996–2000.
- [59] W.J. King, A.C.C. Tseung, *Electrochim. Acta* 19 (1974) 485–491.
- [60] C.F. Windisch, G.J. Exarhos, K.F. Ferris, M.H. Engelhard, D.C. Stewart, *Thin Solid Films* 45 (2001) 398–399.
- [61] M.S. Wu, C.Y. Huang, K.H. Lin, *J. Power Sources* 186 (2009) 557–564.
- [62] A.S. Adekunle, K.I. Ozoemena, *Electroanalysis* 23 (2011) 971–979.